A fully coupled thermomechanical 3D model for all phases of friction stir welding

M. Hossfeld

Rapid Technic AG, Killwangen, Switzerland

E-mail: fsw@rapid.ch

April 2016

Abstract. Although friction stir welding (FSW) has made its way to industrial application particularly in the last years, the FSW process, its influences and their strong interactions among themselves are still not thoroughly understood. The lack of understanding mainly arises from the adverse observability of the actual process with phenomena like material flow and deposition, large material deformations plus their complex thermo-mechanical interactions determining the weld formation and its mechanical properties. A validated numerical process model may be helpful for closing this gap as well as for an isolated assessment of individual influences and phenomena. Hereby such a model will be a valuable assistance for process and especially tool development.

In this study a Coupled Eulerian-Lagrangian (CEL) approach with Abaqus V6.14 is used for modeling the whole FSW process within one continuous model. The resolution reached allows not only simulating the joining of two sheets into one and real tooling geometries but also burr and internal void formation. Results for temperature fields, surface and weld formation as well as process forces are shown and validated.

1. Introduction

Object of the present work is to simulate all stages of the FSW process within one continuous FE model. Therefore a fully coupled thermomechanical 3D model has been developed using the CEL-algorithm of Noh and Abaqus V6.14 [1, 2]. In previous work [3, 4] we found out that this combination was able to deal with the big challenges of modeling FSW that derive from the working principle with non-linear phenomena like material flow, friction and other complex interactions. Furthermore, the simulation of joining two separate sheets into one was possible as well as a detailed prediction of resulting surface geometry and joining zone. This research paper expands named simulation method towards real tool geometries and an extended experimental validation. Furthermore, compared to earlier work most predefined boundary conditions and assumptions could be eliminated or replaced by experimental results.

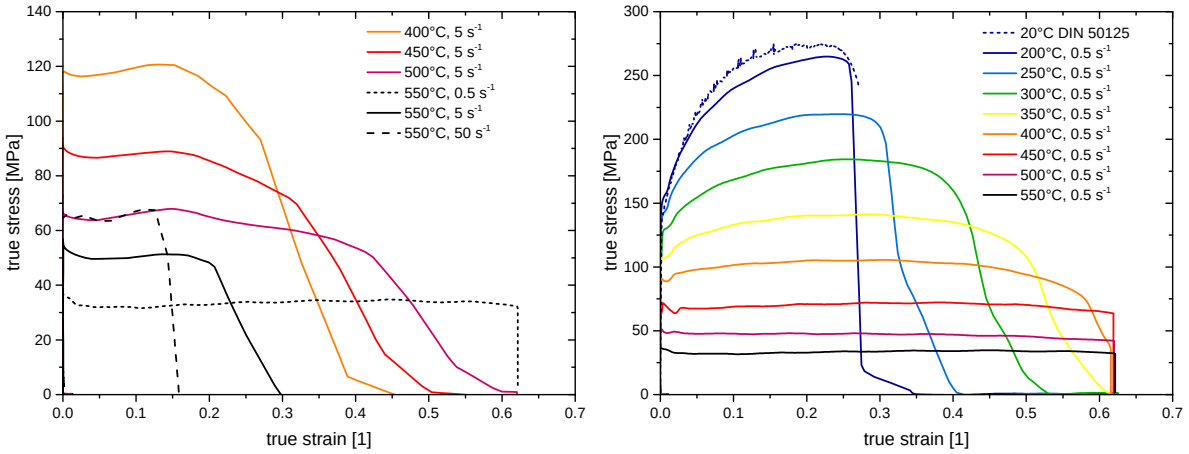

Figure 1: excerpt from mechanical testing done at process-oriented conditions for AA 5182-0. left: strain rate level of $0.5\,\mathrm{s}^{-1}$ for different temperatures. right: material behavior at elevated temperatures and strain rates

2. Modeling material and frictional behavior

Unlike other welding processes, all process phenomena of the working principle during FSW like friction, resulting heat input or material flow are caused and established by mechanical (inter-) actions only. Those actions in turn are the response of the material to the carried out welding process and result in many well-known FSW features, e. g. self-stabilization. Because of that a deep understanding of the material and its behavior is a key element for understanding the FSW process itself.

For describing the material and frictional behavior in the simulation extensive characterizations were done. Because this work focusses on the simulation method for the process, only a rough overview of those experimental procedures is given in the following. However a detailed documentation is provided in German in [5]. With AA 5182-0 and AA 6061-T6 two basically different types of aluminum alloys were investigated. Their mechanical properties were gathered by performing tensile tests at process-oriented temperatures and strain rates using Gleeble systems. Figure 1 gives an insight to those results for AA 5182-0. To provide a good comparability to usual FE modeling the popular semi-empiric visco-plastic Johnson-Cook material model [6] was used to describe the material behavior for this work. It is given by

$$\sigma_{\mathrm{y,J\text{-}C}}(\varepsilon_{\mathrm{v,pl}}\,,\dot{\varepsilon}_{\mathrm{v,pl}}\,,T) = \left[A + B(\varepsilon_{\mathrm{v,pl}})^n\right]\left[1 + C\ln(\dot{\varepsilon}^*_{\mathrm{v,pl}})\right]\left[1 - (T^*)^m\right] \tag{1}$$

$$\text{with} \qquad \dot{\varepsilon}^*_{\mathrm{v,pl}} := \frac{\dot{\varepsilon}_{\mathrm{v,pl}}}{\dot{\varepsilon}_{\mathrm{v,pl,0}}} \qquad \text{and} \qquad T^* := \frac{T - T_0}{T_{\mathrm{S}} - T_0} \tag{2}$$

The material law describes the yield stress $\sigma_{\mathrm{y,J\text{-}C}}$ as a function of effective plastic strain $\varepsilon_{\mathrm{v,pl}}$ and strain rate $\dot{\varepsilon}_{\mathrm{v,pl}}$ as well as temperature T. A, B, C, n, m, $\dot{\varepsilon}_{\mathrm{v,pl,0}}$, T_{S} and T_0 are test or material constants.

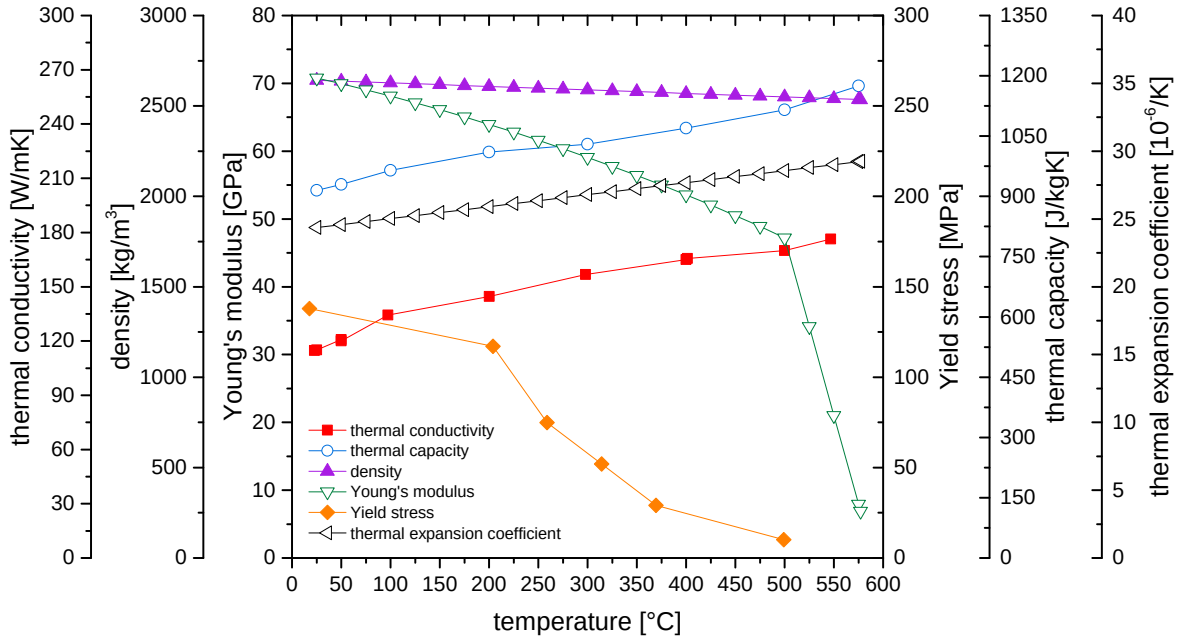

Figure 2: trends of thermic and mechanical properties for AA 5182-0 as a function of temperature, partially with data from [7, 8, 9, 10, 11]

The thermal properties of the alloys with respect to temperature were derived by experiments, taken from literature or calculated by means of physical correlations, e. g. Wiedemann-Franz law. For AA 5182-0 the thermo-physical properties with respect to the temperature are shown in Figure 2.

For assessing the contact behavior between tool and workpiece during FSW isolated frictional experiments were carried out. Therefore tool alike hollow cylinders with different shapes were brought into contact with aluminum sheets that were equipped with thermocouples from underneath. The measurement of the forces was done locally by a telemetric tool holder with 1700 Hz to gather machine unaffected data, Figure 3. Overall 130 friction experiments with different normal pressures, spindle speeds, geometries and contact areas were executed. A more detailed describtion can be found in [5] as well. In general, the experiments showed an self-similar frictional behavior. Figure 4 shows an example with stepwise increasing normal pressure. Initially the system is dominated inherently by friction on oxide or absorption layers. Because of the hard and durable aluminum oxides low or medium pressures and/or velocities result in a only moderate wear of those layers. Therefore no metallic contact between tool and base aluminum occurs, while to some extent the behavior is related to the well-known Coulomb's law, experiments R 90 to R 94 in Figure 4. With increasing pressure or velocity the wear of the outer layers increases up to a point where those are distrubted and a break-in of the tool takes place (R 95). By this a metallic contact between aluminum and tool is established what causes an abrupt rise of forces respectively friction coefficient, heat input and temperatures. In the shown example the heat flow density increases from 5 $\mathrm{W/mm^2}$ to almost 15 $\mathrm{W/mm^2}$ by what the temperature rises from 175 C

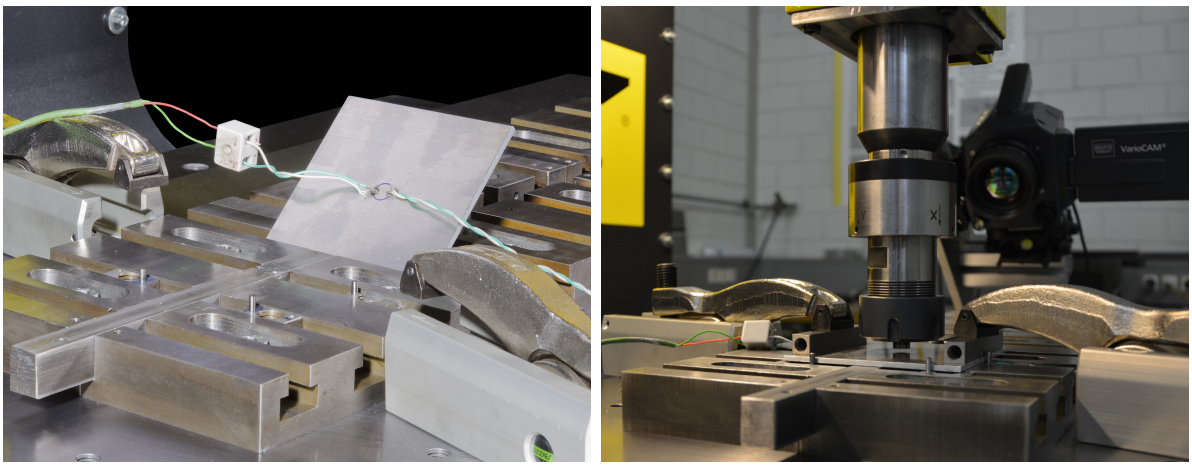

Figure 3: frictional experimental: application of workpiece with thermocouples and experimental setup with telemetric system, infrared camera and machine

to 425 C. Hereby the aluminum softens significantly and finally sticks to the tool causing a self-enhancing effect on wear-in, heat input and also adhesion. Corresponding to the real FSW process temperature and forces stabilize quickly.
After the transition the frictional interface ist strongly dominated by the material behavior showing a manifest multi layer shearing (MLS) of the aluminum [5]. Because of that the friction during FSW is not directly coupled to influences like normal force and has to be expressed in dependence of temperature, interface velocity and stress state. To provide this as well as a numerical stable implemention for this work an visco-plastic friction law based on the Johnson-Cook material model was used to describe the equilibrium of shearing stresses at the contact interface

$$\tau_{\text{friction}} = \frac{1}{\sqrt{3}}\sigma_{y,J-C} \tag{3}$$

$$= \frac{1}{\sqrt{3}}\sigma_y(\varepsilon_{\text{v,pl}}\ , \dot{\varepsilon}_{\text{v,pl}}\ , T) \tag{4}$$

3. Model

The basic model is composed of two eulerian workpieces and a lagrangian tool, adjacent parts like anvil and fixture are modeled as lagrangian bodies as well. A schematic model is shown in Figure 5, the setup in Abaqus/CAE including mesh and a example tool geometry is Figure 6.

To enable the interaction between all parts independent and overlapping meshes of eulerian and lagrangian formulation were used. The eulerian mesh is carried out in a way so that it is well exceeding all designated contact areas with lagrangian bodies. This allows a free material flow within the eulerian mesh after deformation and prevents numerical diffusion efficiently.

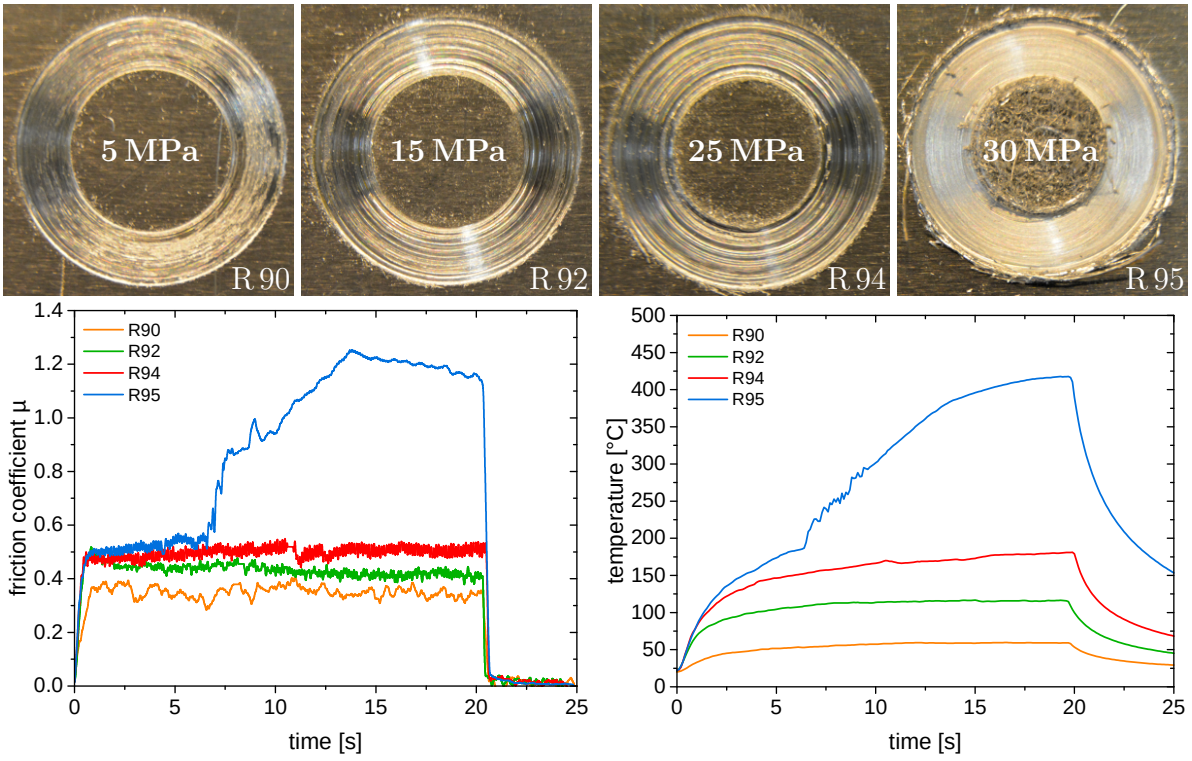

Figure 4: Example of wear in and surface evolution as well as friction coefficient and temperature trends for a test series. Hollow cylinder with 10 / 16 mm inner / outer diameter. $n = 500\,\mathrm{min}^{-1}$ and different average contact pressures

3.1. workpieces

The two workpieces lay within the eulerian mesh and are represented by partially filled cells (volume of fluid method), Figure 5. Due to this approach and the surface reconstruction the representation of the process phenomena in the simulation is strongly linked to the mesh fineness. Therefore, the eulerian mesh includes 230 000 thermally coupled linear elements with reduced integration. For separating the two workpieces and for a more stable handling of contact and friction the later contact and respective joining zone is meshed even finer (red arrow in Figure 6).

3.2. tool

The tool is represented by a linear-elastic lagrangian body with the respective material properties. The representation is limited to the actual tool itself. Spindle shaft and machine are represented by thermal and mechanical boundary conditions.
Simple rotationally symmetric tool geometries can be represented by under-integrated brick elements like C3D8RT. More complex tools e.g. with flutes or structures have to be represented by fully-integrated elements like due to the higher level of detail as well as the higher requirements for describing friction and contact. For example the tool shown in Figure 6 consists of almost 700 000 elements of type C3D4T. Because a real

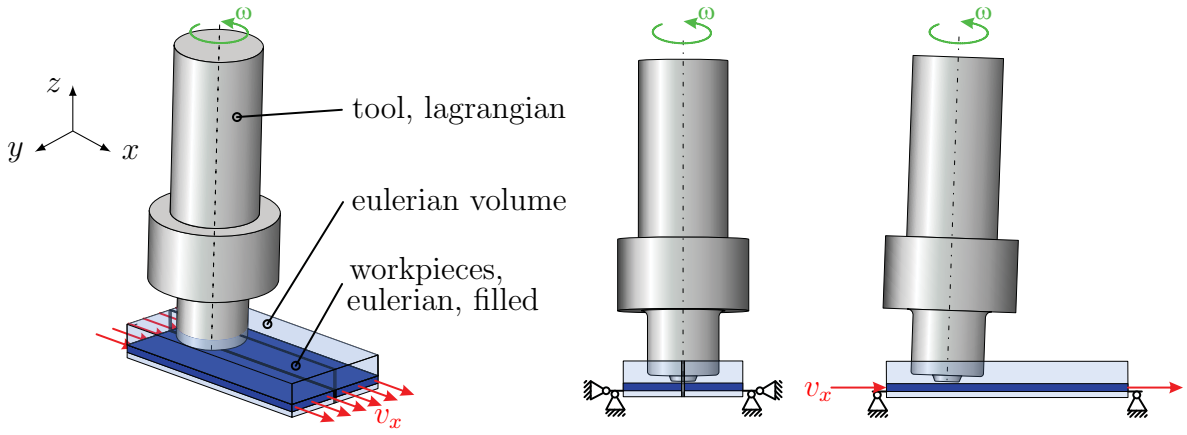

Figure 5: Schematic model assembly. isometrical, front and side view. Illustrated without fixture, anvil and tool shank

tool geometry with flutes can be used for the simulation an active material transport within the volume of revolution is possible, e. g. the pin shown in Figure 6 has a ratio V_{rotation} / V_{pin} of 1.15.

3.3. simulation and implemention of process parameters

Process parameters are implemented on the one hand with the help of a reference point on the tool's center axis (movement or forge force in z, spindle speed etc). Through this point properties like machine stiffness in x, y, z can be realized e.g. by spring constraints. On the other hand the traverse speed v_x is realized by velocity constraints on the eulerian volume (in and out flow), see Figure 5.

For simulating the process the rotating tool plunges in a first step along the z axis until the desired depth is reached. This position is held until the end of the dwelling step. Then the traverse speed is applied on the eulerian volume (ramp) and and if applicable the mode is switched to the virtually force control. After the desired length of the weld is reached the traverse movement is stopped by decreasing in and out flow speed to zero, then the tool is extracted from the joining zone again.

4. Results (excerpt)

4.1. weld geometry and process range

A feasible way to evaluate the quality of the simulation is to compare the surface formation during the pluging step to experiments. This is because the plunging step represents the highest gradient in FSW with a lot of transitions initiated or taking place like contact and friction or material softening and flow which are strongly interacting and linked to many (later) central process phenomena.
Figure 7 shows a comparison during the pluging step in experiment and simulation. As shown all named phenomena evolve in the simulation according to reality and are

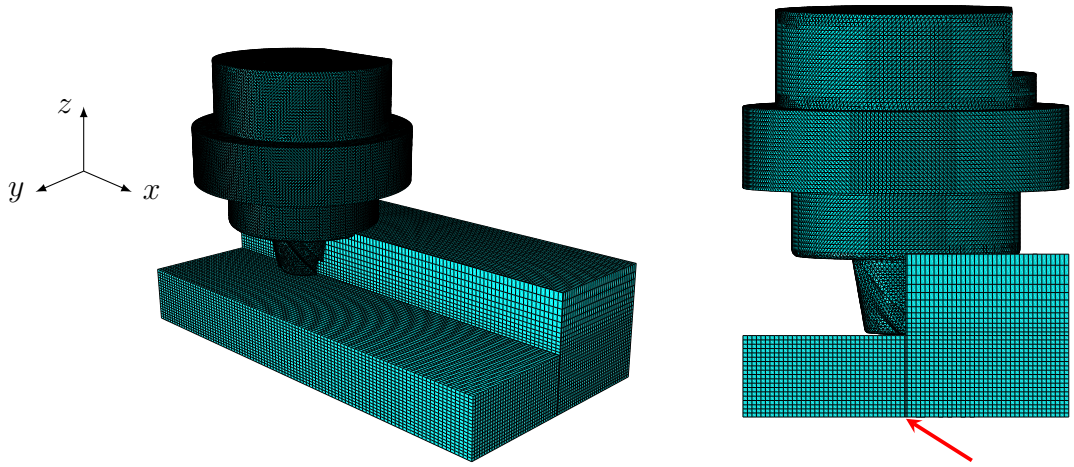

Figure 6: Model assembly in simulation with mesh. isometrical and back view. partially transparent eulerian volume

represented well. Even some more detailed events like the joint line dissolution (Fig. 7a) or the formation of little "flakes" and the lip (Fig. 7c) can be predicted by the simulation. An extended view of the fully plunged tool and a comparison with the process range predicted in the simulation is given in Figure 8.

4.2. microstructure

Directly linked with the effective process range is the evolution of the microstructure. Like shown in earlier work a quick and good estimate of size, shape and zones can be made based on the accumulated strain [12, 3, 4]. This is primarily because the continuous dynamic recrystallization (CDRX) can only occur where the material is deformed to a quite high extend while it is simultaneously exposed to elevated temperatures. Because of the self-stabilizing features of the process those two phenomena are mutually dependent and result in the typical locally very limited process with high strain gradients between Nugget, TMZ and base material. It should be mentioned that by this the microstructure evolution is of course a function of the welded material. An example for a microstructure prediction and named circumstance is given in Figure 9.

4.3. forces and temperature fields

Process forces can be directly read out on the reference point after the simulation. An overview of detail and quality is given in Table 1. While the mean values match quite well, minimum and maximum values differ. This can be lead back to the very different sampling rate between simulation and experiment. Nevertheless, all simulation results lay within the spread of the raw data of the telemetric system what is plausible.
A comparison of temperature fields and heat propagation of the related weld provides Figure 10. In this context the asymmetric propagation along the joint line and the warmer advancing side should be mentioned what correlates well with experiments.

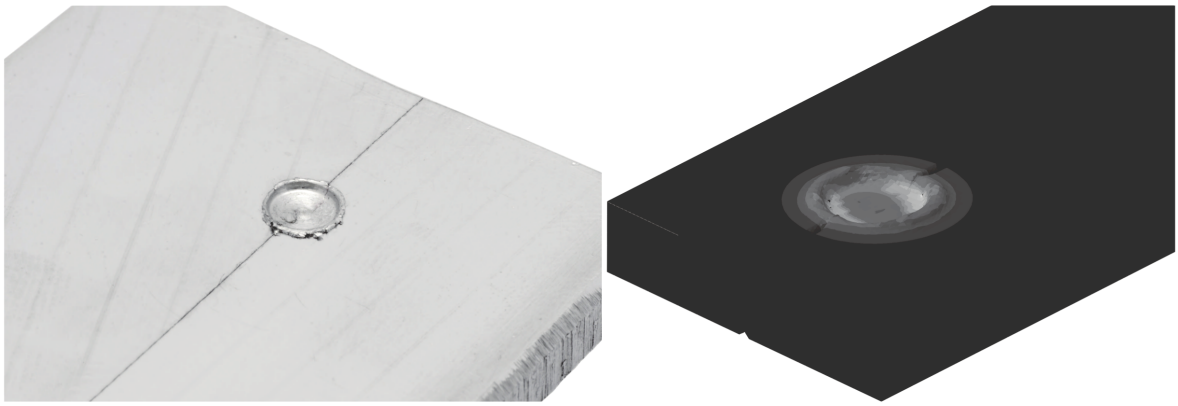

(a) 0.5 mm plunging depth: distortion of joint line

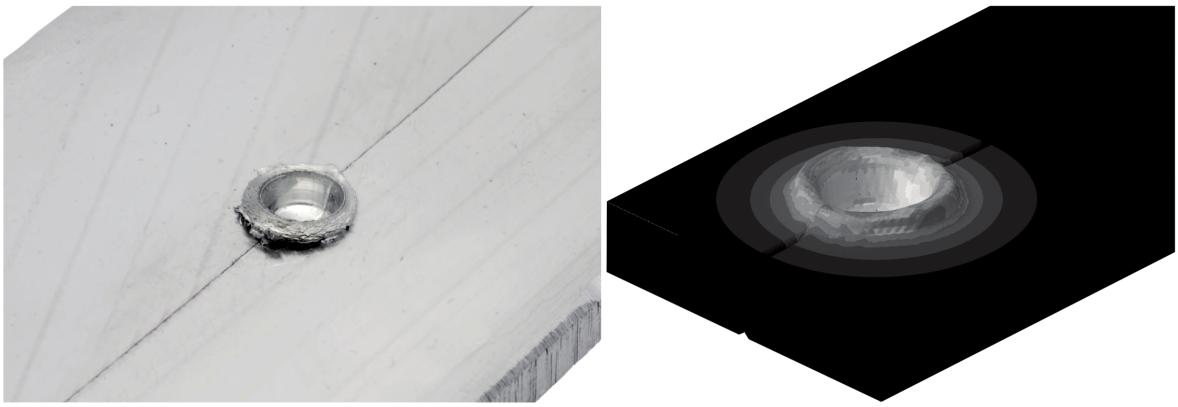

(b) 3 mm plunging depth: formation of a "cup" with lip

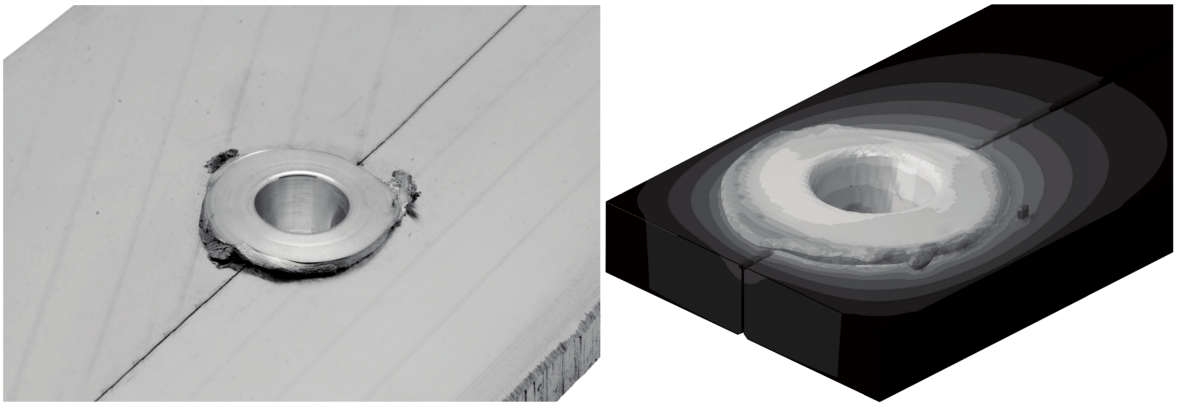

(c) 4.8 mm plunging depth: everting material as the shoulder touches

Figure 7: evolution of the weld geometrie during plunging in experiment (left) and simulation (right) in 5 mm EN AW-6061–T6 and the tool shown in Figure 6.

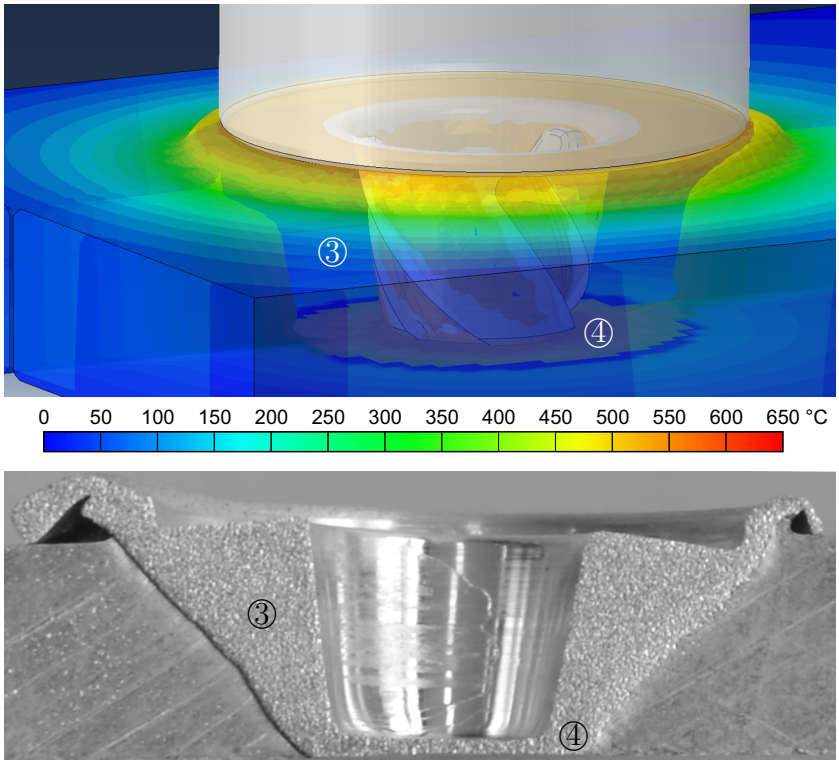

Figure 8: material flow and process range ③, pressure distribution below the tool on anvil ④: plunged tool with active structures and traverse cut of experiment

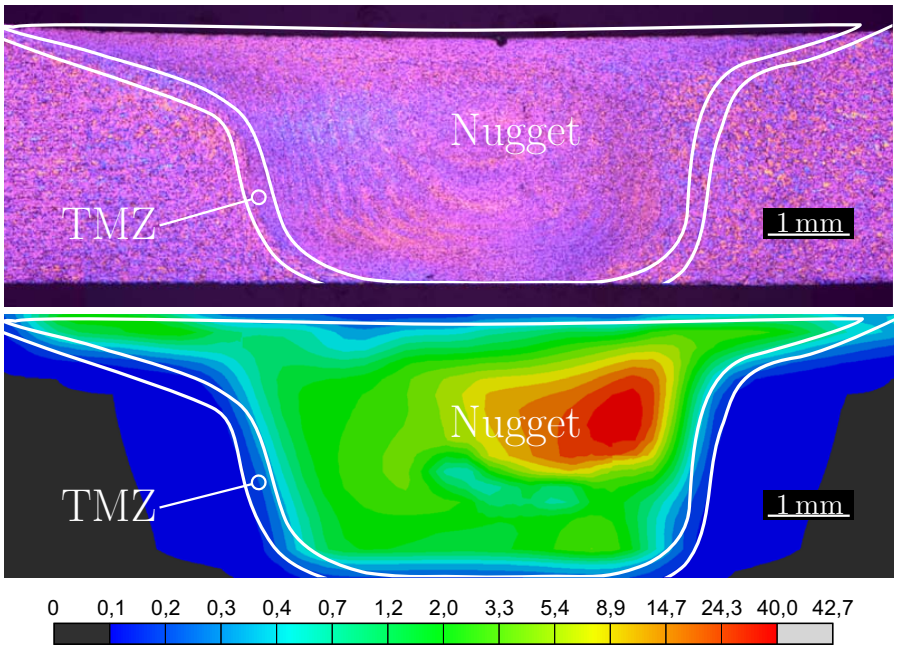

Figure 9: representation of weld geometry and microstructure. macro section and simulation result (plastic equivalent strain). White accentuation for better perceptibility.

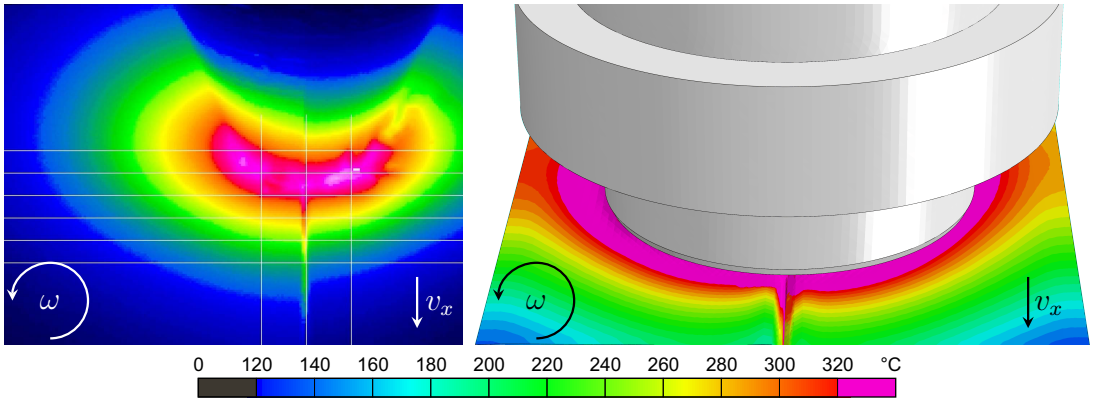

Figure 10: comparison of temperature field in experiment (left) and simulation (right). Asymetrical heat propagation on advancing and retreating side.

Table 1: comparison of process forces of the stationary state. Simulation average of 60 values / 1.5 sec, experiment of 2040 values / 1.2 sec. Min/Max experiment: raw data of telemetric system (1700 Hz)

		experiment	simulation	difference	
				absolute	relative
F_z	max	9920 N	8723 N	−1197 N	−12.0 %
		8240 N	**8023 N**	**−217 N**	**−2.6 %**
	min	7062 N	7278 N	+216 N	+3.0 %
F_x	max	1439 N	1317 N	−122 N	−8.4 %
		1000 N	**998 N**	**−2 N**	**−0.2 %**
	min	727 N	801 N	+74 N	+10.2 %
M	max	19.8 Nm	18.1 Nm	−1.7 Nm	−8.6 %
		14.0 Nm	**16.5 Nm**	**+2.5 Nm**	**+17.8 %**
	min	6.0 Nm	15.1 Nm	+9.1 Nm	+151.7 %

5. Summary

During this work the FSW process could be brought back to its underlying physics while most assumptions and simplifications could be avoided. Based on the quantification of the central process phenomena a 3D FE simulation method was developed that is able to simulate real joint and detailed tool geometries and can predict material flow, void and burr formation as well as process forces.

Acknowledgement

The author acknowledges support given by Deutsche Forschungsgemeinschaft (DFG) in Project DFG RO 651/16-1 that was carried out at the Material Testing Institute (MPA) at the University of Stuttgart.

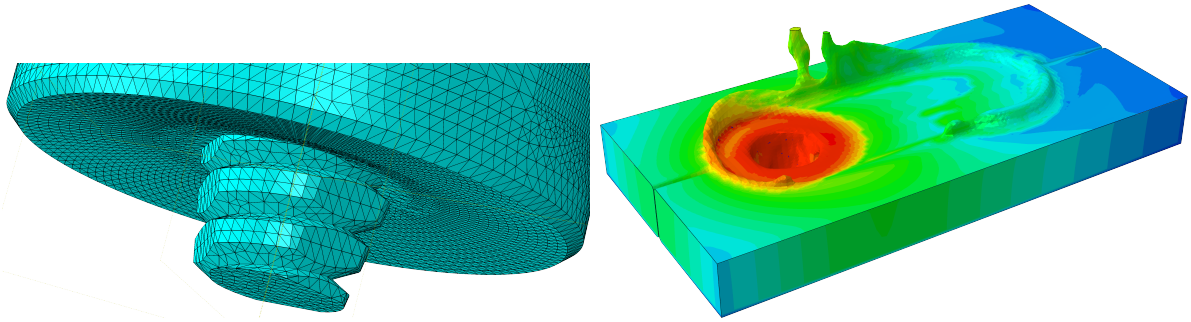

Figure 11: left: level of tool detail reached in this study, right: welding of two sheets into one and burr formation due to excessive plunging (tool not shown).

Literature

[1] W. F. Noh. Cel: A time-dependent, two-space-dimensional, coupled eulerian-lagrangian code. *Methods in Computational Physics*, 3:117–179, 1964.

[2] Dassault Systèmes. *Modeling Extreme Deformation and Fluid Flow with Abaqus: V6 R6.12*. Vélizy-Villacoublay, Frankreich, 2012.

[3] M. Hossfeld and E. Roos. A new approach to modelling friction stir welding using the cel method. *Advanced Manufacturing Engineering and Technologies NEWTECH 2013 Stockholm, Schweden*, pages 179–190, 2013.

[4] M. Hossfeld. Modelling friction stir welding: evolution of microstructure and weld geometry of aluminium alloy en aw 6061. *Proceedings of the 39th MPA-Seminar, Stuttgart*, 2013.

[5] M. Hossfeld. *Experimentelle, analytische und numerische Untersuchungen des Rührreibschweißprozesses*. Dissertation, 2016.

[6] G. R. Johnson and W. H. Cook. A constitutive model and data for metals subjected to large strains, high strain rates and high temperatures. *Proceedings of the 7th International Symposium on Ballistics*, 21, 1983.

[7] M. Spittel and T. Spittel. Thermal expansion of light metal alloys. In H. Warlimont, editor, *Part 2: Non-ferrous Alloys - Light Metals*, volume 2C2 of *Landolt-Börnstein - Group VIII Advanced Materials and Technologies*, pages 92–95. Springer, 2011.

[8] D. C. Prasso, J. W. Evans, and I. J. Wilson. Heat transport and solidification in the electromagnetic casting of aluminum alloys: Part i. experimental measurements on a pilot-scale caster. *Metallurgical and Materials Transactions B*, 26(1):1243–1251, 1995.

[9] D. C. Prasso, J. W. Evans, and I. J. Wilson. Heat transport and solidification in the electromagnetic casting of aluminum alloys: Part ii. development of a mathematical model and comparison with experimental results. *Metallurgical and Materials Transactions B*, 26(1):1281–1288, 1995.

[10] K. C. Mills. *Recommended values of thermophysical properties for selected commercial alloys*. Woodhead, Cambridge, 2002.

[11] R. C. Picu, G. Vincze, F. Ozturk, J. J. Gracio, F. Barlat, and A. M. Maniatty. Strain rate sensitivity of the commercial aluminum alloy aa5182-o. *Materials Science and Engineering: A*, 390(1-2):334–343, 2005.

[12] S. Guerdoux and L. Fourment. A 3d numerical simulation of different phases of friction stir welding. *Modelling and Simulation in Materials Science and Engineering*, 17(7):075001, 2009.